J. Appl. Cryst. (1997). **30**, 345–352

Optimization of a Bonse–Hart Ultra-Small-Angle Neutron Scattering Facility by Elimination of the Rocking-Curve Wings

M. AGAMALIAN,[a] G. D. WIGNALL[a] AND R. TRIOLO[b]

[a]*Oak Ridge National Laboratory,† Oak Ridge, TN 37831, USA, and* [b]*University of Palermo, Via Archirafi 26, 90123-Palermo, Italy. E-mail: triolo@mbox.unipa.it*

(*Received 21 August 1996; accepted 19 November 1996*)

Abstract

The ORNL Ultra-Small-Angle Neutron Scattering (USANS) facility at the High Flux Isotope Reactor (HIFR) has been recently upgraded, using the Bonse–Hart technique. Si(111) triple-bounce channel-cut single crystals have been used for both the monochromator and analyzer. The total width of the rocking curve of the analyzer is about 1.6″ and the wavelength of the primary neutron beam is 2.59 Å. It has been demonstrated that, owing to the low neutron absorption of silicon, the wings of the rocking curve are generally contaminated by neutrons propagating and diffracting inside the walls of channel-cut crystals. This parasitic intensity has been eliminated by the cutting of a groove in the long wall and the insertion of a cadmium absorber (0.6 mm thick). This modification effectively suppresses the wings of the rocking curve by over two orders of magnitude and thus dramatically improves the sensitivity of the diffractometer. The upgraded facility has been tested with several samples, including a polystyrene latex with a radius of 2.50×10^4 Å as determined by optical microscopy. The average radius calculated from USANS data is 2.48×10^4 Å, in excellent agreement with independently determined dimensions. The minimum accessible scattering vector of the upgraded USANS facility is $Q_{min} \simeq 2 \times 10^{-5}$ Å^{-1}, which corresponds to a maximum resolvable real-space dimension of $2\pi/Q_{min} \simeq 3 \times 10^5$ Å (30 μm).

1. Introduction

Over the past two decades, small-angle neutron scattering (SANS) has become one of the most widely used techniques for the study of superatomic structure in condensed matter. Conventional pinhole SANS instruments cover a range of scattering vectors $10^{-3} < Q < 1$ Å^{-1} ($Q = 4\pi\lambda^{-1}\sin\theta$, where λ is the wavelength and 2θ is the scattering angle) and thus the maximum measurable distance in real space is $\sim 10^3$ Å. For example, in the case of dilute solutions of individual particles (*e.g.* macromolecules), the upper limit of the radius of gyration (which is one of the most general parameters for describing such systems) is typically $R_g \simeq 500$–600 Å, *via* the limit of the Guinier approximation ($QR_g \leq 1$). Thus, large inhomogeneties, such as aggregates of macromolecules, polymer latexes, magnetic domains, various fibers and micelles, and many other objects, are beyond the resolution limit of conventional pinhole SANS facilities, and a different methodology based on the utilization of perfect crystals for SANS measurements (Mook, 1974) is required to cover the ultra-small-Q range $10^{-5} < Q < 10^{-3}$ Å^{-1}. The first USANS studies were carried out in the 1970s (Kalanov, Shil'shtein & Somenkov, 1974; Christen, Tasset, Spooner & Mook, 1977) and the systematic development of the technique continued throughout the 1980s, as several types of double-crystal diffractometers (DCDs) using perfect crystals were designed (Bader, Rauch & Zeilinger, 1982; Schwahn, Mikšlovsky, Rauch, Seidl & Zugaret, 1985; Treimer, Berger, Rucket & Seidl, 1987; Kulda & Mikula, 1983; Mikula, Lukas & Eichhorn, 1988; Treimer, Strothman, Semioschkina & Scheit, 1989; Mikula, Lukas, Kulda & Eichhorn, 1989). DCDs currently operate in the US (Christen *et al.*, 1977; Popovici, Yelon & Berliner, 1995), Austria (Mikšlovsky, Amenitch, Rauch & Seidl, 1992), Germany (Schwahn *et al.*, 1985; Hempel & Eichhorn, 1995), Japan (Aizawa & Tomimitsu, 1995; Takahashi & Hasimoto, 1995) and Russia (Abov, Elyutin, Matveev & Eidlin, 1994). This wide geographical spread reflects the growing interest in USANS structural studies.

The underlying principle of USANS DCDs is similar to ultra-small-angle X-ray scattering (USAXS) facilities, and both are based on an extremely highly correlated beam that undergoes Bragg reflection from a perfect crystal. Following the Ewald theory (Zachariasen, 1967), the total width of the reflection curve of perfect crystals is typically several arcseconds or even less, which creates the opportunity of measuring extremely small angles. The Bragg reflectivity of a perfect crystal is very high ($\sim 98\%$), but the intensity of the reflected

† Managed by Lockheed Martin Energy Research Corporation for US Department of Energy under contract number DE-AC05-960R22464.

neutron beam is low owing to the small wavelength spread, and this constitutes a serious limitation for USANS instruments. This problem has been discussed (Treimer *et al.*, 1989) and a DCD with a multicrystal system measuring several identical rocking curves simultaneously has been designed and tested. Similarly, a DCD with four monochromator/analyzer crystals with a consequent fourfold intensity gain has been described by Treimer *et al.* (1987). The possibility of using a position-sensitive detector to measure several points of the rocking curve simultaneously has also been explored, and two types of analyzer crystal, a bent silicon crystal (Mikula, Lukas & Eichhorn, 1988) and a bent comb-shaped crystal (Niel, Rauch, Seidl, 1991), have found application in the USANS instrument. Probably the most convenient and optimal solution of the intensity problem has been found for medium-resolution DCDs or the two-bent-crystal technique (Kulda & Mikula, 1983; Mikula, Lukas & Eichhorn, 1988; Mikula *et al.*, 1989; Popovici, Yelon & Berliner, 1995) making it possible to achieve the intensity gain by the bending of both of the crystals and the application of a position-sensitive detector.

Another strategy to optimize the USANS instruments is to improve the sensitivity and ultimate resolution of DCDs by employment of the Bonse–Hart technique (Bonse & Hart, 1965), which was originally implemented in ultra-small-angle X-ray scattering (USAXS) instruments. In this case, channel-cut triple-bounce crystals are used as monochromator and analyzer crystals (Schwahn *et al.*, 1985; Mikšlovsky *et al.*, 1992) to suppress the wings of the rocking curve, which leads to a significant increase in the signal-to-background ratio of the DCDs. However, comparison of the rocking curves of a Bonse–Hart DCD in the vicinity of $2\theta \simeq 10''$ shows that the efficiency of suppression of wings is about two orders of magnitude less for neutrons (Schwahn *et al.*, 1985; Mikšlovsky *et al.*, 1992) compared to X-rays (Bonse & Hart, 1965). This discrepancy represents the main drawback of application of Bonse–Hart collimation to USANS instruments and the removal of this limitation is the focus of the present study.

2. Adaptation of the Bonse–Hart technique for USANS and suppression of the wings of the rocking curve

The ORNL USANS instrument is installed at the HB-3A horizontal beamline of the High Flux Isotope Reactor (HFIR). Fig. 1 shows the original layout of the facility (Christen *et al.*, 1978) with two single-bounce Si(111) crystals (single-/single-bounce scheme). Also shown is the new layout, where the monochromator and the analyzer are both replaced by triple-bounce Si(111) crystals (triple-/triple-bounce scheme). The primary neutron beam is reflected from an Si(111) mosaic crystal, then from an Si(111) premonochromator (perfect crystal), and enters the Bonse–Hart (multiple-bounce) DCD. The wavelength of the primary-beam is $\lambda = 2.59$ Å and the cross section at the sample position is 2×4 cm. USANS studies are usually undertaken with the measurement two rocking curves (with and without a sample), the first of which $[I_s(Q)]$ contains useful structural information *via* diffraction from inhomogeneities in the sample, together with the instrumental background. The second signal $[I_b(Q)]$ contains only the background, and the USANS curve corresponding to diffraction from inhomogeneities of a sample is the difference between these two measurements: $I(Q) = I_s(Q) - I_b(Q)$, with a statistical error $\pm [I_s(Q) + I_b(Q)]^{1/2}$. Thus, the rocking curve from an empty instrument characterizes the sensitivity of the DCD, which can only be increased by suppression of the wings.

The rocking curves corresponding to single-/single-bounce and triple-/triple-bounce schemes are shown in Fig. 2 (curves *A* and *B*, respectively). These data show that the triple-/triple-bounce scheme suppresses the wings by a factor of ~ 10 (at $2\theta = 10''$) compared with the single-/single-bounce geometry. The relative intensity $I(2\theta = 10'')/I(0)$ for the triple-/triple-bounce scheme is $\sim 10^{-3}$, which is similar to that obtained for the other Bonse–Hart neutron instruments (Schwahn *et al.*, 1985; Mikšlovsky *et al.*, 1992). However, this parameter is about two orders of magnitude higher than has been obtained for the X-ray DCD $[(2\theta = 10'')/I(0) \simeq 10^{-5}]$ using five/five-bounce Si(220) channel-cut crystals (Bonse & Hart, 1965). It has also been reported (Schwahn *et al.*, 1985) that nine reflections from three triple-bounce Si(331) crystals still produced a relative suppression of the wings of the rocking curve of only $\sim 10^{-3}$, which is significantly less than expected. Additional measurements were undertaken with the detector in transmission position to clarify this result, and it was found that the rocking curve behind the fifth reflection is split into two peaks (Schwahn *et al.*, 1985). This observation was attributed

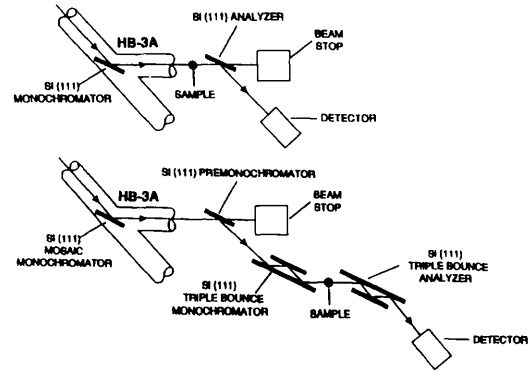

Fig. 1. Single-/single-bounce and triple-/triple-bounce schemes of the ORNL USANS facility.

to imperfections of the lattice of the silicon single crystal, but to our knowledge the lattice imperfection does not affect the USAXS instruments (Bonse & Hart, 1965).

A hypothesis that qualitatively explains the discrepancy between the application of the Bonse–Hart technique for the two types of radiation is based on the much smaller natural absorption of silicon for neutrons (approximately four orders of magnitude) compared with X-rays (Bacon, 1975). Therefore, a component of the neutron-radiation flux is capable of propagating inside the transparent crystal undergoing additional (to the Bragg reflection from the front face of the crystal) diffraction. Several mechanisms operate in this case. The Bragg reflection from the back face should be considered first, because mostly the front and back boundaries of a finite-thickness perfect crystal plate participate in this phenomenon following the dynamic diffraction theory. Thermal diffuse scattering (TDS), experimentally observed from perfect silicon crystals (Graf, Schneider, Freund & Lehmann, 1981; Zeilinger & Shull, 1982), can be named next, and Bragg reflection by crystallites also cannot be neglected. According to this postulate, one would expect that the neutron beam, which is reflected from a triple-bounce channel-cut crystal, should contain the admixture of neutrons that have undergone Bragg diffraction and TDS inside the long wall.

In order to verify this hypothesis, measurement of the rocking curve was undertaken with the short wall of the triple-bounce analyzer-crystal covered by a neutron absorber (cadmium sheet). In this geometry (Fig. 3), only neutrons that undergo propagation and diffraction inside the long wall of the channel-cut crystal can be detected. Fig. 4 shows the corresponding rocking curve (curve *C*) obtained together with the original result (curve *B*). Comparison of the rocking curves with and without the cadmium wafer gives strong support to the above hypothesis, and it may be seen that the component of the neutron flux that is diffracted inside the silicon single crystal is split into two peaks. These (parasitic) neutrons form only a small fraction ($\sim 2\%$) of the integrated intensity but their contribution to the wings is substantial (approximately 90%). Natural absorption suppresses this parasitic component for X-rays, but this is not the case when a conventional channel-cut crystal reflects a neutron beam. We have therefore modified the crystal geometry to eliminate this parasitic component of the reflected beam as indicated in Fig. 5. In order to prevent the propagation of radiation within the transparent crystal, a new channel-cut crystal has been designed and constructed with an additional groove for the cadmium insert in the long wall (Fig. 6). The rocking curve measured by the triple-/triple-bounce scheme with the modified channel-cut crystals is curve *D* in Fig. 2 and shows a significant improvement in performance compared to previous Bonse–Hart USANS instruments (Schwahn *et al.*, 1985; Mikšlovsky *et al.*, 1992). Not only are the wings suppressed by an additional two orders of magnitude, but the parameter $I(2\theta = 10'')I(0) = 2 \times 10^{-5}$ (curve *D* in Fig. 2) is equal to or even exceeds the equivalent (at the same Q) values for USAXS facilities (at $Q = 1.18 \times 10^{-4}$ Å the corresponding angle for copper X-ray radiation is $2\theta \simeq 6''$ owing to the difference in wavelength). It also has to be noted that our result is obtained for the triple-/triple-

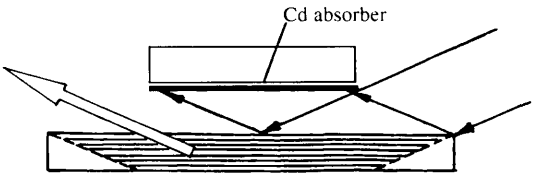

Fig. 3. Geometry of neutrons, Bragg-reflected from upper layers, propagated (shaded zone) and diffracted inside the long wall of the channel-cut crystal. The short wall is covered by the cadmium sheet.

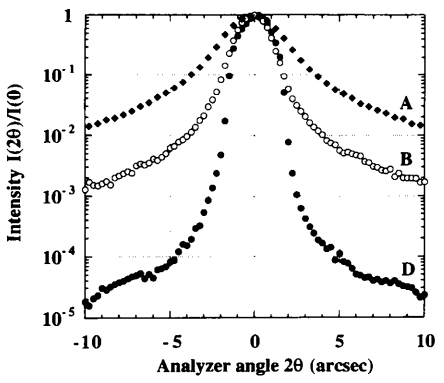

Fig. 2. Rocking curves of the DCD diffractometer: *A* single-/single-bounce scheme; *B* triple-/triple-bounce scheme; *D* triple-/triple-bounce scheme with modified channel-cut crystals containing cadmium insert.

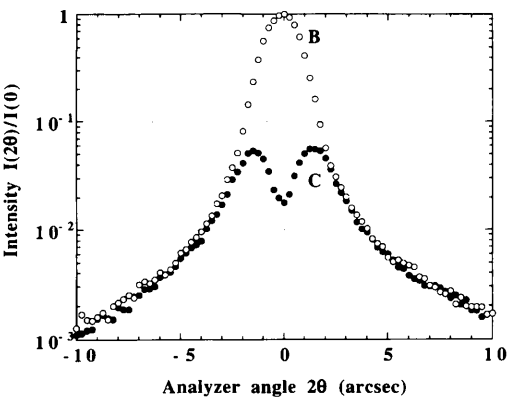

Fig. 4. Rocking curves of the triple-/triple-bounce scheme: *B* as in Fig. 2; *C* short wall of the triple-bounce analyzer-crystal is covered by cadmium sheet (Fig. 3).

bounce scheme (six reflections) in comparison with ten reflections using in the X-ray technique (Bonse & Hart, 1965; Matsuoka & Ise, 1993). Thus, the cadmium insert accomplishes for neutrons what natural absorption does for X-rays and brings the performance of the USANS facility up to the state-of-the-art standard previously set by USAXS instruments.

It is also interesting to compare this experimental result with the rocking curve calculated from the dynamic diffraction theory (Zachariasen, 1967). The rocking curve for a DCD with channel-cut crystals is a convolution of reflectivity curves from each of the crystals:

$$I(\Delta) = \int [R(y)^n [R(y + \Delta]^m \, dy, \tag{1}$$

where n and m are the number of reflections in monochromator and analyzer crystals, respectively, and $R(y)$ can be written by the Ewald formula:

$$\begin{aligned} R(y) &= 1, |y| \leq 1, \\ R(y) &= 1 - (1 - y^{-2})^{1/2} |y| > 1. \end{aligned} \tag{2}$$

The argument y in (1) and (2) is the reduced angular parameter of the dynamic diffraction theory and the plateau ($-1 \leq y \leq 1$) corresponds to the total width of the symmetric reflection curve in angular scale:

$$\Delta\theta = b_c \exp(-W)|F|N\lambda^2/\pi \sin 2\theta_B, \tag{3}$$

where b_c is a coherent length $\exp(-W)$ the Debye–Waller factor, F a geometric structure factor, N the particle density, λ the wavelength and θ_B the related Bragg angle.

The fit is shown in Fig. 7 on a semilogarithmic scale and good agreement is achieved with the Ewald theory in the range $0 \leq 2\theta \leq 2.5''$, where the intensity decreases by three orders of magnitude. The total width of the reflection curve of the triple-bounce Si(111) single crystal for $\theta_B = 2.24°$, determined from the fit, is $\Delta 2\theta = 1.6''$. The departure from the theoretical rocking curve for $2\theta > 2.5''$ may be explained by the same mechanisms of diffraction inside the walls of the modified channel-cut crystals (see shaded zones in Fig. 5) and small-angle scattering from the mechanically damaged surface layer can also make a significant contribution to the intensity of wings at this level of intensity. The phenomenon needs to be explored in more detail for the further improvement of the USANS technique and this study is in progress.

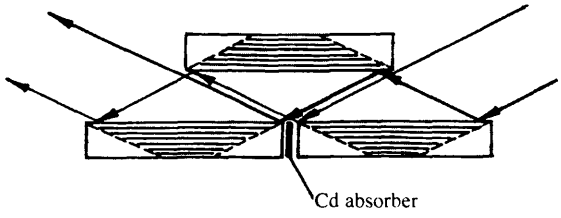

Fig. 5. Geometry of triple Bragg reflection in channel-cut crystal with additional groove and cadmium insert in long wall. The area of diffraction of the neutron wave inside the walls is indicated by shaded zones.

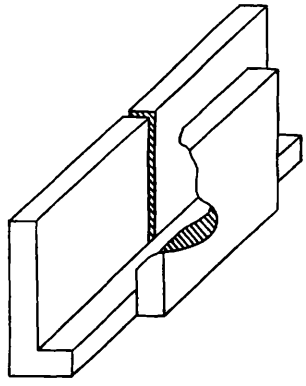

Fig. 6. Design of the channel-cut crystal with additional groove for cadmium absorber.

3. Instrumental performance and calibration standards

3.1. *Polymer latexes*

An aqueous suspension of polystyrene latexes with a nominal diameter of 5.0 μm (determined by optical microscopy) was used as a standard to calibrate the upgraded ORNL USANS facility. The sample was contained in a quartz cell (1.0 × 1.8 × 3.6 cm) and, although the concentration was low (0.06 vol% in D_2O), the experimental scattering curve $I(Q)$ was easily

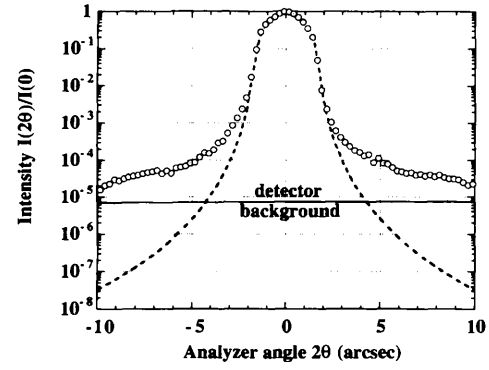

Fig. 7. Experimental rocking curve for triple-/triple-bounce scheme with modified channel-cut crystals with cadmium insert (D in Fig. 2) and fit to the Darwin theory (dashed line). The solid line is detector background.

resolved and fitted to a model of polydisperse solid spheres:

$$I_{th}(Q) \simeq \int N(R)R^6F(QR)\,dR, \quad (4)$$

where $N(R)$ is a numerical size distribution function and $F(QR)$ is the form factor of a solid sphere of radius R:

$$F(QR) = 9[(\sin QR - QR\cos QR)/(Q^3R^3)]^2. \quad (5)$$

The distribution function $N(R)$ is chosen as the double Gaussian function because of the admixture of small particles, which usually presents in the suspension of polystyrene latexes obtained by emulsion polymerization. Collimation corrections have been performed by double convolution of the theoretical scattering function $I_{th}(Q)$ [(4)] with horizontal $W_h(t)$ and vertical $W_v(u)$ collimation functions of the instrument (Feigin & Svergun, 1987):

$$I_{sm}(Q) = \int\int W_h(t)W_v(u)I_{th}\{(2\pi/\lambda) \times [(2\theta - t)^2 + u^2]^{1/2}\}\,du\,dt, \quad (6)$$

where $I_{sm}(Q)$ is the smeared scattering function, t and u are the horizontal and vertical angular coordinates respectively and $W_h(t)$ and $W_v(u)$ obey the normalization condition:

$$\int W_h(t)\,dt = \int W_v(u)\,du = 1. \quad (7)$$

$W_h(t)$ is the rocking curve of the empty USANS instrument and $W_v(u)$ is the distribution of the primary-beam intensity along the vertical axis of the detector plane, convoluted with the vertical aperture of the detector. Fig. 8 shows the form factor of a solid sphere $F(QR)$, derived for the radius $R = 2.5 \times 10^4$ Å directly from (5), together with the smeared form factor $F_{sm}(QR)$ calculated by (6). This example shows that subsidiary maxima of the form factor $F(QR)$ (curve A) are clearly resolved after the collimation smearing owing to the ultra-high angular resolution in the horizontal plane (curve B), but the intensity in zero angle is significantly reduced by the slit-geometry factor $A_{sg}(R) = F_{th}(0)/F_{sm}(0) = 5 \times 10^2$, which depends on the size of calibration standard. The latter effect is connected with the very high (relatively to the horizontal) vertical divergence of the primary-beam and must be taken into account when the absolute scale coefficient is calculated.

The experimental and calculated data from the latex solution are shown in Fig. 9, together with the size distribution function $N(R)/N(R_m)$ normalized to unity at the peak of the main mode R_m. The average radius $\langle R\rangle = 2.48 \times 10^4$ Å, calculated for the function $N(R)$, is consistent with that obtained by optical microscopy ($\langle R\rangle = 2.50 \times 10^4$ Å).

Absolute calibration of the intensity scale is accomplished from the expression for the intensity at zero angle:

$$I_{th}(0) = 16/9\pi^2(\Delta\rho)^2 \int N(R)R^6\,dR, \quad (8)$$

where $\Delta\rho$ is a contrast between the polystyrene and D_2O, and the numerical size distribution function $N(R)$ obeys the normalization condition:

$$4/3\pi \int N(R)R^3\,dR = \varphi, \quad (9)$$

where φ is the volume fraction of polystyrene latexes in the solution. The absolute calibration coefficient C_{abs} is calculated from the ratio of the intensity at zero angle, measured experimentally and corrected for the slit geometry factor $A_{sg}(R) = F_{th}(0)/F_{sm}(0)$, measuring time t and transmission of sample T_s, and calculated theoretically:

$$C_{abs} = I_{exp}(0)A_{sg}(R)/I_{th}(0)T_st. \quad (10)$$

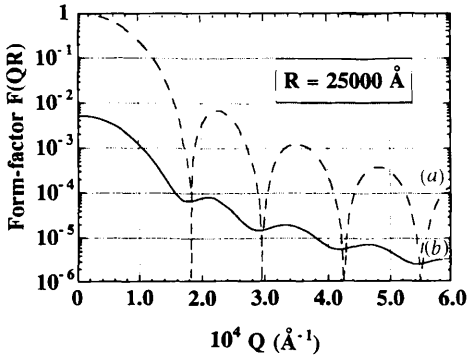

Fig. 8. Form factor of solid sphere of radius $R = 25000$ Å, calculated (a) without and (b) with collimation smearing.

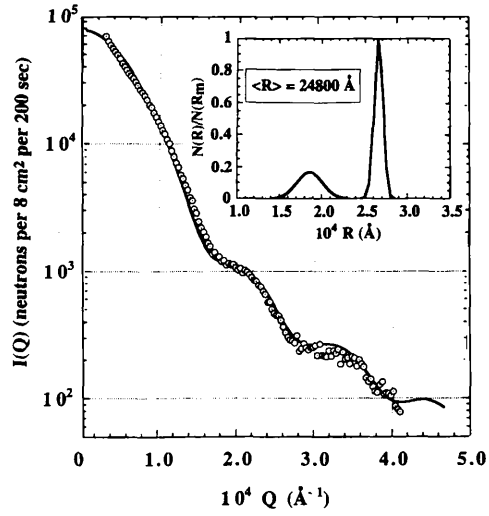

Fig. 9. Fit to the model of polydisperse solid spheres and the corresponding numerical distribution function $N(R)$. The solid line is the smeared scattering function $I_{sm}(Q)$.

The coefficient C_{abs}, defined by (10), depends only on the geometrical parameters of the USANS instrument and the primary-beam intensity, but not on the size of the calibration standard.

3.2. *Polymer blends*

It is well established (Alamo *et al.*, 1997; Graessley *et al.*, 1994; Krishnammorti, Graessley, Balsara & Lohse, 1994; Nicholson, Finerman & Crist, 1990; Rhee & Crist, 1991) that SANS can be used to determine the melt compatibility of mixtures of linear and branched polyolefins, including high-density (HD) and linear low-density (LLD) polyethylenes. HDPE is the most crystalline form of polyethylene (PE) because the chains are linear and contain virtually no branching. LLDPE is produced by catalytical copolymerization of ethylene with an α-olefin such as butene or hexene and can have a wide range of branch contents, depending on concentration of added comonomer. SANS data indicate (Graessley *et al.*, 1994; Krishnamoorti *et al.*, 1966) that mixtures of HDPE and LLDPE are homogeneous in the melt when the branch content is low (*i.e.* <3 branches/100 backbone carbons). However, when the branch content is higher (>10 branches/100 backbone carbons for a molecular weight of $\sim 10^5$), the blends phase separate (Alamo *et al.*, 1997). For a typical LLDPEs prepared with heterogeneous-type Ziegler–Natta catalysts, the multisite nature of catalysts used leads to a wide distribution of chain compositions (Nesarikar & Crist, 1994) and thus must be thought of as 'blend' of different species. When the composition distribution is broad enough, the multicomponent system can, in principle, phase separate. This raises the possibility that even when the average branch content is low, there should be a small fraction of highly branched chains (*e.g.* >10 branches/100 backbone carbons), which are incompatible with the lightly branched molecules and will thus phase separate, as suggested by Mirabella and co-workers (Mirabella & Ford, 1987; Mirabella, Westphal, Fernando, Ford & Williams, 1988). Previous SANS studies (Wignall, Alamo, Londono, Mandelken & Stehling, 1996) of heterogeneous ethylene–hexene LLDPE copolymers have confirmed the existence of a dispersed minority phase. Xylene extraction removes the highly branched molecules and hence the volume fraction of the disperse phase (ϕ) is higher in the extracted material. However, these experiments were conducted using a pinhole SANS facility with an upper resolution limit of $\sim 10^3$ Å, whereas microscopy indicates that the dimension of the disperse phase may extend to the μm range. We have therefore complemented those initial investigations with USANS, which increases the spatial resolution by a factor of ~ 30; Fig. 10 shows the overlap of the pinhole SANS and USANS data.

The volume fraction of the disperse phase can be estimated (Wignall, 1996) from the SANS invariant:

$$Q_0 = \int Q^2 d\sum/d\Omega(Q)\, dQ = 2\pi^2 \phi_1 \phi_1 \phi_2 [\rho_{1n} - \rho_{2n}]^2, \quad (11)$$

where ϕ_1, ϕ_2 and ρ_{1n}, ρ_{2n} are the volume fractions and neutron scattering-length densities of the two phases, respectively, and scattering contrast is obtained between the phases by blending 20% deuterated HDPE (HDPE-D) with the protonated LLDPE. On the basis of previous studies, the linear material should be incompatible with the minority phase, but should mix homogeneously with the predominantly low-branched matrix (Alamo *et al.*, 1997). Thus, the addition of HDPE-D should provide SANS contrast between the phases (and also between the protonated and deuterated molecules within the majority phase), without perturbing the predicted two-phase morphology. Fig. 11 shows the Kratky plot of the combined pinhole-SANS/USANS data for $T = 433$ K and the area under this curve is the invariant Q_0 [(12)],

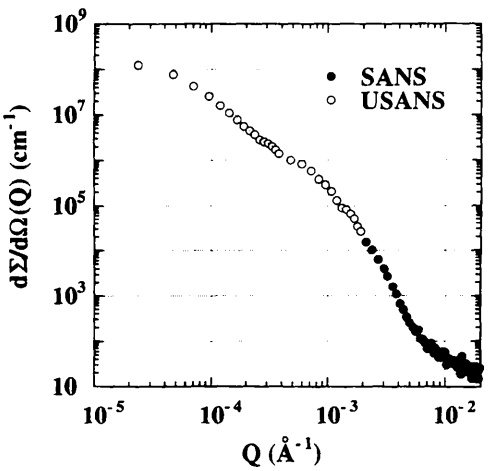

Fig. 10. Overlap of SANS and USANS data obtained for 20% linear HDPE-D blended with branched LLDPE-H at $T = 433$ K.

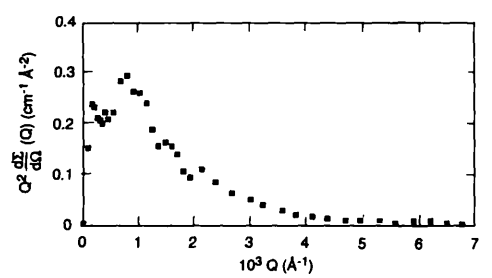

Fig. 11. Kratky plot of combined SANS/USANS data obtained at $T = 433$ K for 20% linear HDPE-D blended with branched LLDPE-H.

which leads to a volume fraction of the disperse phase of $\phi = 0.30$. This may be compared with the previous determination ($\phi = 0.20$) derived from the pinhole SANS data with $Q_{min} \simeq 4 \times 10^{-3}$ Å^{-1}, which was extrapolated to $Q = 0$ *via* the Guinier approximation (Wignall, 1966). Thus, USANS substantially improves the estimate of ϕ by filling in the previously inaccessible portion of the SANS invariant.

3.3. *Polycapillary fibers*

Polycapillary fibers (Chen *et al.*, 1992) with a diameter of 0.4 mm made from lead-silica glass have been used to test the resolution of the upgraded ORNL USANS facility, as applied to the measurement of a diffraction pattern from a regular periodic structure. Each fiber contains more than 1000 capillaries of an internal diameter of 7 μm, creating a two-dimensional hexagonal structure (see microphotograph insert in Fig. 12) with the distance between neighboring channels $a = 11$ μm, determined by electron microscopy. The USANS data (Fig. 12) have been obtained from a stack of fibers with dimensions 0.4 × 10 × 40 mm oriented perpendicular to the diffraction plane. The distance between neighboring channels, calculated from the position of the first diffraction maxima [$Q = 6.54 \times 10^{-5}$ Å^{-1}, $a = (4\pi/3^{1/2} \times Q_1^{-1} = 11.09$ μm], is consistent with that determined by electron microscopy. The diffraction pattern from a hexagonal structure can be indexed by the sequence of peaks observed in the experimental curve. However, a complete analysis of the data is not trivial, owing to the complicated shape of the network, created by the channels and holes in between the neighboring channels (see microphotograph in Fig. 12) and interfiber interference.

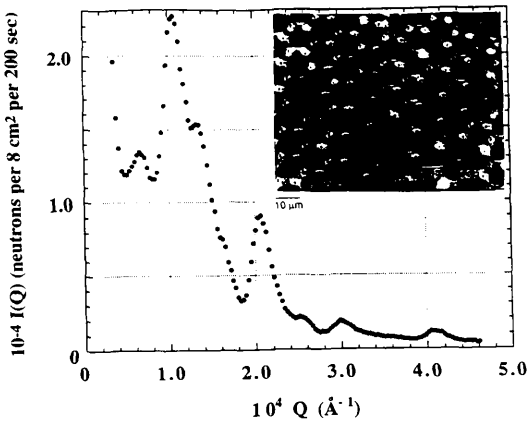

Fig. 12. Diffraction pattern from polycapillary glass fibers, measured by the ORNL USANS instrument and electron microphotograph, obtained by Chen *et al.* (1992).

4. Summary

The comparison of the experimentally measured rocking curves for X-rays and neutron Bonse–Hart DCDs reveals a significant (about two orders or magnitude) difference in the intensity of the wings of the rocking curve. This problem has been studied by the ORNL USANS facility, indicating that the wings of the rocking curve are contaminated by neutrons that have undergone Bragg reflections and TDS inside the long wall of the channel-cut crystals. In the case of X-rays, this intensity is suppressed by the natural absorption of the material, which explains the lower intensity of the wings of the rocking curve for X-ray Bonse–Hart instruments. The new triple-bounce channel-cut crystal with additional groove for a cadmium absorber in the middle of the long wall has been designed for USANS instruments to cut out this neutron intensity. This modification solves the problem of the wings of the rocking curve and improves significantly (by about two orders of magnitude) the sensitivity of USANS cameras, making this parameter even better than that for USAXS instruments.

The authors thank H. A. Mook (ORNL) and C. J. Glinka (National Institute of Standards and Technology) for their interest in the present study and for fruitful discussions. We are also grateful to D. F. R. Mildner (National Institute of Standards and Technology) for the samples of polycapillary fibers and to J. Colopus (ORNL) for technical help with the reconstruction of the channel-cut crystals. The research at Oak Ridge was supported by the Division of Material Science, US Department of Energy under Contract No. DE-AC5-96OR22464 with Lockheed Martin Energy Research Corporation. This research was supported in part by an appointment to the Oak Ridge National Laboratory Postdoctoral Research Associates Program administered jointly by the Oak Ridge National Laboratory and the Oak Ridge Institute for Science and Education.

References

Abov, Yu. G., Elyutin, N. O., Matveev, D. C. & Eidlin, A. O. (1994). *Pribori i Teknika Eksperimenta*, **6**, 67–79. (In Russian.)

Aizawa, K. & Tomimitsu, H. (1995). *Physical (Utrecht) B*, **213&214**, 884–886.

Alamo, R. G., Londono, J. D., Mandelkern, L., Stehling, F. C. & Wignall, G. D. (1994). *Macromolecules*, **27**, 411–419.

Alamo, R. G., Graessley, W. W., Krishnamoorti, R., Lohse, D. J., Londono, J. D., Mandelkern, L., Stehling, F. C. & Wignall, G. D. (1997). *Macromolecules*, **30**, 561–567.

Bacon, G. E. (1975). *Neutron Diffraction*. Oxford: Clarendon Press.

Bader, D., Rauch, H. & Zeilinger. A. (1982). *Z. Naturforsch.* **37A**, 512–516.

Bonse, U. & Hart, M. (1965). *Appl. Phys. Lett.* **7**, 238–240.

Chen, H., Downing, R. G., Mildner, D. F. R., Gibson, W. M. Kumakov, M. A., Ponomarev, I. Yu. & Gubarev, M. V. (1992). *Nature (London)*, **357**, 391–393.

Christen, D. K., Tasset, F., Spooner, S. & Mook, H. A. (1977). *Phys. Rev. B*, **15**, 4506–4509.

Feigin, L. A. & Svergun, D. I. (1987). *Structural Analysis by Small-Angle X-ray and Neutron Scattering*. New York: Plenum Press.

Graessley, W. W., Krishnamoorti, R., Balsara, N. P., Fetters, L. J., Lohse, D. J., Schultz, D. N. & Sissano, J. A. (1994). *Macromolecules*, **26**, 1137–1142; **27**, 2574–2583, 3073–3080, 3896–3903.

Graf, H. A., Schneider, J. R., Freund, A. K. & Lehmann, M. S. (1981). *Acta Cryst.* A**37**, 863–871.

Hempel, A. & Eichhorn, F. (1995). *BENSC Experimental Report*, HM1-B525, p. 350.

Kalanov, M., Shil'shtein, S. S. & Somenkov, V. A. (1974). *Sov. Phys. Crystallogr.* **18**, 755–757.

Krishnamoorti, R., Graessley, W. W., Balsara, N. & Lohse, J. D. (1994). *Macromolecules*, **27**, 3073–3087.

Kulda, J. & Mikula, P. (1983). *J. Appl. Cryst.* **16**, 489–504.

Matsuoka, H. & Ise, N. (1993). *Chemtracs-Macromolecular Chemistry*, Vol. **4**, pp. 59–72.

Miksovsky, A., Amenitch, H., Rauch, H. & Seidl, E. (1992). *Phys. Status Solidi A*, **130**, 365–372.

Mikula, P., Lukas, P. & Eichhorn, F. (1988). *J. Appl. Cryst.* **21**, 33–37.

Mikula, P., Lukas, P., Kulda, J. & Eichhorn, F. (1989). *Physica (Utrecht) B*, **156&157**, 605–607.

Mirabella, F. M. & Ford, E. A. (1987). *J. Polymer Sci. Polymer Phys. Ed.* **25**, 777–785.

Mirabella, F. M., Westphal, S. P., Fernando, P. L., Ford, E. A. & Williams, J. G. (1988). *J. Polymer Sci.* B**26**, 1995–2007.

Mook, H. A. (1974). *J. Appl. Phys.* **45**, 43–46.

Nesarikar, A. & Crist, B. (1994), *J. Polymer Sci.* B**32**, 641–652.

Nicholson, J. C., Finerman, T. & Crist, B. (1990). *Polymer*, **31**, 2287–2295.

Niel, L., Rauch, H. & Seidl, E. (1991). *J. Appl. Cryst.* **24**, 562–567.

Popovici, M., Yelon, W. B. & Berliner, R. (1995). *J. Phys. Chem. Solids*, **56**, 1425–1431.

Rhee, J. & Crist, B. C. (1991). *Macromolecules*, **24**, 5665–5678.

Schwahn, D., Miksovsky, A., Rauch, H., Seidl, E. & Zugarek, G. (1985). *Nucl. Instrum. Methods*, A**239**, 229–234.

Takahashi, T. & Hashimoto, M. (1995). *Phys. Lett. A*, **200**, 73–75.

Treimer, W., Berger, G., Ruckert, B. & Seidl, E. (1987). *Z. Phys. B*, **68**, 527–536.

Treimer, W., Strothmann, H., Semioschkina, N. & Scheib, H. (1989). *Physica (Utrecht) B*, **156&157**, 598–601.

Wignall, G. D. (1996). *Physical Properties of Polymers. Handbook*, edited by J. E. Mark, pp. 299–310. Woodbury, NY: American Institute of Physics.

Wignall, G. D., Alamo, R. G., Londono, J. D., Mandelkern, L. & Stehling, F. C. (1996). *Macromolecules*, **29**, 5332–5339.

Zachariasen, W. H. (1967). *Theory of X-ray Diffraction in Crystals*. New York: Dover.

Zeilinger, A. & Shull, C. G. (1982). Paper presented at conference, *The Neutron and its Applications*, Cambridge, England, September 13–17. Unpublished.